

## Article

# Dynamic Response Characteristics of Composite Concrete Structures Subjected to Reactive Jet Impact

Chenghai Su, Peiyu Li, Jiahao Zhang, Aoxin Liu, Yuanfeng Zheng  and Haifu Wang \* 

State Key Laboratory of Explosion Science and Technology, Beijing Institute of Technology, Beijing 100081, China; 3120205123@bit.edu.cn (C.S.); 3120225089@bit.edu.cn (P.L.); 3120215138@bit.edu.cn (J.Z.); 3120225099@bit.edu.cn (A.L.); zhengyf@bit.edu.cn (Y.Z.)

\* Correspondence: wanghf@bit.edu.cn

**Abstract:** Composite concrete structures, commonly found in urban infrastructures, such as highways and runways, are pivotal research object in the protection field. To study the dynamic response of composite concrete structures subjected to reactive jet penetration coupled with an explosive effect, a full-scale damage experiment of composite structures under the action of 150 mm caliber shaped charges was performed, to derive the dynamic damage modes of different concrete thicknesses under the combined kinetic and chemical energy damage effects. The results indicated that under aluminum jet penetration, concrete layers exhibited minor funnel craters and penetration holes. However, concrete layers displayed a variety of damage modes, including central penetration holes, funnel craters, bulges, and radial/circumferential cracks when subjected to the PTFE/Al jet. The area of the funnel crater expanded as the thickness of the concrete increased, while the height of the bulge and the number of radial cracks decreased. The diameter of penetration holes increased by 76.9% and the area of funnel crater increased by 578% in comparison to Al jet penetration damage. A modified-RHT concrete model that reflected concrete tensile failure was established, utilizing AUTODYN. Segmented numerical simulations of damage behavior were performed using the FEM-SPH algorithm and a restart approach combined with reactive jet characteristics. The spatial distribution characteristic of the reactive jet and the relationship between kinetic penetration and explosion-enhanced damage were obtained by the simulation, which showed good concordance with the experimental results. This study provides important reference data and a theoretical basis for the design of composite concrete structures to resist penetration and explosion.

**Keywords:** composite concrete structures; concrete layer; penetration; explosion; dynamic damage



**Citation:** Su, C.; Li, P.; Zhang, J.; Liu, A.; Zheng, Y.; Wang, H. Dynamic Response Characteristics of Composite Concrete Structures Subjected to Reactive Jet Impact. *Buildings* **2024**, *14*, 624. <https://doi.org/10.3390/buildings14030624>

Academic Editors: Ricardo Castedo, Weifang Xiao and Maria Chiquito

Received: 4 February 2024

Revised: 22 February 2024

Accepted: 24 February 2024

Published: 27 February 2024



**Copyright:** © 2024 by the authors. Licensee MDPI, Basel, Switzerland. This article is an open access article distributed under the terms and conditions of the Creative Commons Attribution (CC BY) license (<https://creativecommons.org/licenses/by/4.0/>).

## 1. Introduction

In modern urban and military constructions, composite concrete structures are widely utilized due to their exceptional mechanical properties and durability [1]. These structures not only fulfill basic architectural functions but also play a crucial role in protection design. With the evolution of modern warfare and urban security threats, improving the protective capacity of composite concrete structures against high-speed impact and explosive loads has arisen as a research focus [2].

Composite concrete structures typically consist of multiple layers, including concrete, gravel layer, compacted soil, and foundation. These structures are widely used in various facilities such as building foundations, roads, and airport runways. The strength of the concrete layer determines the functionality and resistance of the structure against damage [3]. The complexity of the explosive damage mechanisms and the damage processes inside the composite concrete structures necessitate the description of multiple effect parameters [4,5]. However, conducting large-scale repetitive experiments is time-consuming and costly. Consequently, some researchers have investigated the dynamic response of single-layer concrete media under explosive effects [6–8], typically employing numerical simulations,

small-charge experiments, or a limited number of full-scale experiments, combined with dimensional analysis to investigate the issues related to internal explosion damage in concrete and develop engineering models. Westine et al. used a similarity analysis to establish a damage model of explosive-damaged runways, which can be used to predict the response pattern, true crater size, and extent of concrete cracking [9]. Through simulation experiments, Wang et al. obtained experimental data on the damage effect of multi-layer media under different charges and burial depths, and used dimensional analysis to derive the functional expression of the damage effect of blasted concrete layers in multi-layer media [10]. Wan et al. first used projectiles to penetrate a scaled concrete target; they buried explosives in the target, and conducted damage assessment on the airport runway scaled target through experiments and numerical simulations [11]. However, internal explosions in composite concrete structures involve a series of problems, such as nonlinear structural response and high strain rate effects, while currently related studies are scarce. More complexly, as a typical protective structure, composite concrete structures must withstand various modes of damage, such as combined penetration and explosion damage. Due to the complexity of penetration and explosion mechanisms, current research has mostly focused on single-type damage from penetration or explosion [12–14].

The development of new energetic materials introduces new challenges in the penetration and explosion resistance of composite concrete structures. Reactive materials based on polytetrafluoroethylene (PTFE), such as PTFE/Al, PTFE/Ti, PTFE/Cu, and PTFE/Al/W, possess certain mechanical strengths and can release chemical energy upon impact, initiating quasi-explosive reactions and releasing a significant amount of gaseous products. Over the past two decades, these materials have been widely applied in defense, aerospace, and civilian fields [15,16]. With the growing prevalence of reactive materials, numerous scholars have conducted a series of studies on PTFE-based reactive materials, including their mechanical properties [17,18] and energy-release characteristics [19,20]. Liners made from reactive materials can form high-speed reactive jets under the shaped charges effect, capable of both penetrating and exploding. Preliminary research on the combined penetration–explosion damage behavior of reactive jets has been undertaken by scholars such as Baker et al. [21], who conducted an experimental study on the influence of reactive liner shaped charges on concrete targets under different oxygen content states, in comparison with aluminum jets. Experimental results showed that, compared with pure metal jets, the damage effect of reactive jets on concrete targets was significantly enhanced. Daniels et al. [22] announced the technological research progress of reactive liner shaped charges. At 1.0 times the stand-off, the diameter of the crater caused by the shaped charges with a diameter of 216 mm on the simulated airport runway was approximately 1.5 m. Xiao et al. [23,24] further investigated the penetration and explosion against multi-layer concrete targets by reactive jets and provided formulas for calculating crack lengths. Zhang et al. [25] used the SPH numerical simulation method and the explosion experiment research to simulate the continuous dynamic damage behavior of the reactive jet that can penetrate the concrete target before exploding. The numerical simulation results were consistent with the experimental results, and the reactive liner showed significant damage-enhancement effect. These previous studies have shown that the combined penetration and explosion damage of concrete structures by reactive jets is a brand-new phenomenon that requires in-depth analysis and discussion of its dynamic damage mechanism. Nevertheless, neither the dynamic response mechanisms of composite concrete structures under the combined action of jet penetration and explosion, nor the relationship between kinetic penetration and explosion enhancement, have been clarified in the preliminary experimental studies on the effects of reactive jets on concrete structures.

Therefore, building on previous research, this paper analyzes the dynamic damage mechanism of composite concrete structures under the combined action of reactive jet penetration and explosion. The influence mechanism of different concrete layer thicknesses on the damage effect of reactive jet was obtained. The paper firstly carries out three full-scale damage experiments on composite structures of varying concrete layer thicknesses

under the action of 150 mm caliber reactive shaped charges, obtaining typical dynamic damage patterns of composite concrete structures under the combined action of reactive jet penetration and explosion. Subsequently, the damage effects of reactive and inert jets were compared in an experiment using an inert Al jet. This study analyzes the dynamic coupling mechanism of penetration damage and explosion-enhanced damage in composite concrete structures through segmented numerical simulation utilizing the FEM-SPH (Finite Element and Smoothed Particle Hydrodynamics) numerical algorithm, introducing the reaction delay time of the reactive jet, and employing a modified-RHT that better reflects the tensile failure of concrete. This provides important reference data and a theoretical basis for the anti-destruction design of composite concrete structures.

## 2. Material and Methods

### 2.1. Material Preparation

#### 2.1.1. Preparation of Composite Concrete Structures

Airport runway is a typical composite concrete structure [11], which is generally composed of multiple composite concrete structures of the same size. A common single block of airport runway has a side length of  $5\text{ m} \times 5\text{ m}$ , and the concrete layer thickness is generally 200 mm–500 mm. Therefore, a composite concrete structure was built as shown in Figure 1, divided into a concrete layer, a cement stabilized gravel layer, and a compacted soil layer, with each layer measuring  $5\text{ m} \times 5\text{ m}$ .

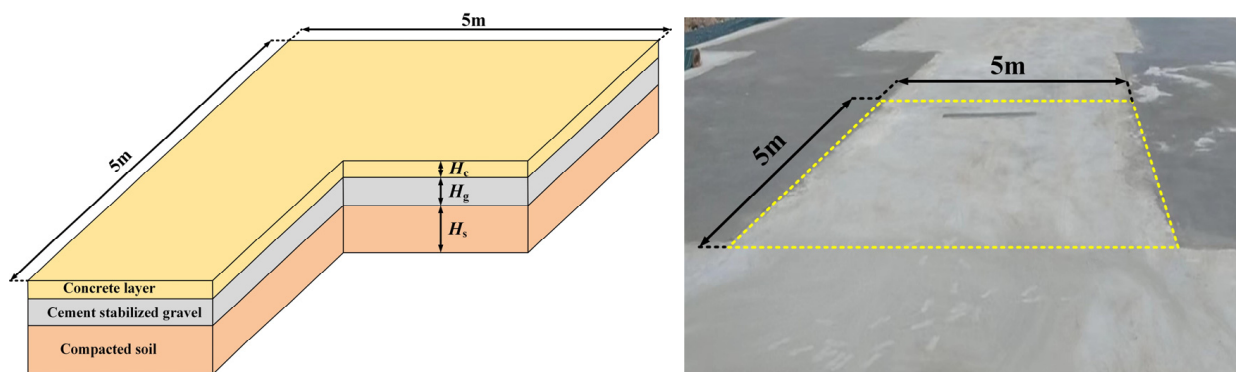


**Figure 1.** Composite concrete structure.

(1) The concrete layer was designed with a compressive strength of C35, with thicknesses ( $H_c$ ) of 250 mm, 350 mm, and 450 mm. The cement used was ordinary Portland cement with low shrinkage, high wear resistance, and good freeze-thaw resistance, having a specific surface area of 300–450  $\text{m}^2/\text{kg}$  and a 28-day shrinkage rate of no more than 0.10%. Natural sand with less than 3% mud content was selected for the aggregate; gravel materials were used in a graded manner, with the maximum particle size not exceeding 40 mm, as specified in Table 1. The curing period for the graded concrete layer was no less than 28 days, and the compressive strength and flexural strength tests were performed using  $150\text{ mm} \times 150\text{ mm} \times 550\text{ mm}$  beam specimens that were cast simultaneously. Table 2 shows the results of the three tests, and the average of the three test results was used as the compressive strength and flexural strength of the concrete layer.

(2) The thickness ( $H_g$ ) of the cement-stabilized gravel layer was 40 cm, using the same grading method as the concrete layer, with the maximum particle size not exceeding 40 mm and a cement content of 5.0%. The layer was mechanically compacted to more than 96% compaction degree, with a designed compressive strength of 6 MPa.

(3) The compacted soil layer consisted of clayey soil, sourced locally, with a thickness ( $H_s$ ) of  $\geq 70\text{ cm}$  and a compaction degree of  $\geq 96\%$ .

**Table 1.** Particle composition of graded gravel material.

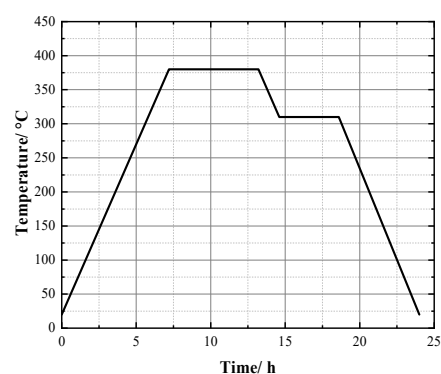
Sieve pore size (square/mm)	2.36	4.75	9.5	19	31.5	37.5	Liquid limit
Mass fraction (%)	0–35	17–45	29–59	54–84	93–100	100	<28

**Table 2.** Compressive strength and flexural strength tests of the concrete layer.

Specimen Number	Test Compressive Strength (MPa)	Average Compressive Strength (MPa)	Test Flexural Strength (MPa)	Average Flexural Strength (MPa)
1	47.8		5.1	
2	46.7	47.3	5.1	5.1
3	47.4		5.1	

### 2.1.2. Preparation of the Reactive Liner

The PTFE/Al reactive material not only possesses a certain mechanical strength but also releases chemical energy under impact. The reactive liner is crushed under the detonation of shaped charges and forms a jet internally and a slug externally, creating a significant velocity gradient across the reactive jet, which leads to jet stretching. Studies have shown [20,26] that the reaction of the reactive jet is a typical process of force-thermal-chemical coupling. The decomposition of the matrix material requires time, and there needs to be a certain growth process for the reaction between the decomposition products and the aluminum powder before a violent explosion occurs. This means that the explosive reaction of the reactive jet is delayed, which allows it to form a jet on a macro scale and utilize its kinetic energy for penetration. The reaction delay time,  $\tau$ , is the interval between the impact on the reactive liner and the instantaneous violent explosion. The chemical reaction of the reactive jet before this delay time is often disregarded, assuming the reactive jet is completely inert before its delay time,  $\tau$ , and explodes instantaneously when the time reaches  $\tau$ . The reactive liner material used in this study consisted of a mixture of 73.5% PTFE (DuPont, type MP 1500 J, Wilmington, DE, USA) and 26.5% Al (Hunan Goldsky Aluminum Industry High-Tech Co., Ltd., Changsha, China, JT-4), with a density of approximately 2.27 g/cm<sup>3</sup> and a total mass of 1080 g. The preparation process was divided into three steps: (1) Powder Mixing: After initial mixing, the powder was further mixed in a special ball mill for three hours, then the thoroughly mixed powder was dried in a vacuum oven at 82 °C for about 24 h; (2) Cold Pressing: The required mass of the reactive material for the liner was calculated, the mixed and dried powder material was weighed, poured into a prepared mold, and pressed under a pressure of 300 MPa for 30 s. The cold-pressed liner sample was then left under an ambient pressure and temperature for 24 h to remove any internal air and residual stress; (3) Sintering: The cold-pressed liner sample was placed in a nitrogen-filled sintering furnace for sintering. The sintering temperature curve is shown in Figure 2 [27], with a maximum temperature of 380 °C, and the liner sample was cooled to room temperature in the furnace afterwards.

**Figure 2.** Sintering temperature curve.

The reactive liner samples were subjected to Scanning Electron Microscope (SEM) imaging and Energy Dispersive Spectroscopy (EDS) elemental analysis, with the results shown in Figure 3. The EDS surface scan elemental analysis results are presented in Table 3. After magnification by 250 times under the SEM, it was observed that the interfaces between the PTFE particles disappeared after sintering, forming a continuous hole, which enhanced the mechanical properties of the material. The PTFE matrix encapsulated Al particles, with the aluminum particles having an approximate diameter of 30  $\mu\text{m}$ . According to the results of the elemental analysis by EDS scanning, besides carbon (C), fluorine (F), and aluminum (Al), the sample also contained a small amount of oxygen. This was attributed to the formation of a dense oxide layer on the surface of the aluminum powder upon contact with air.

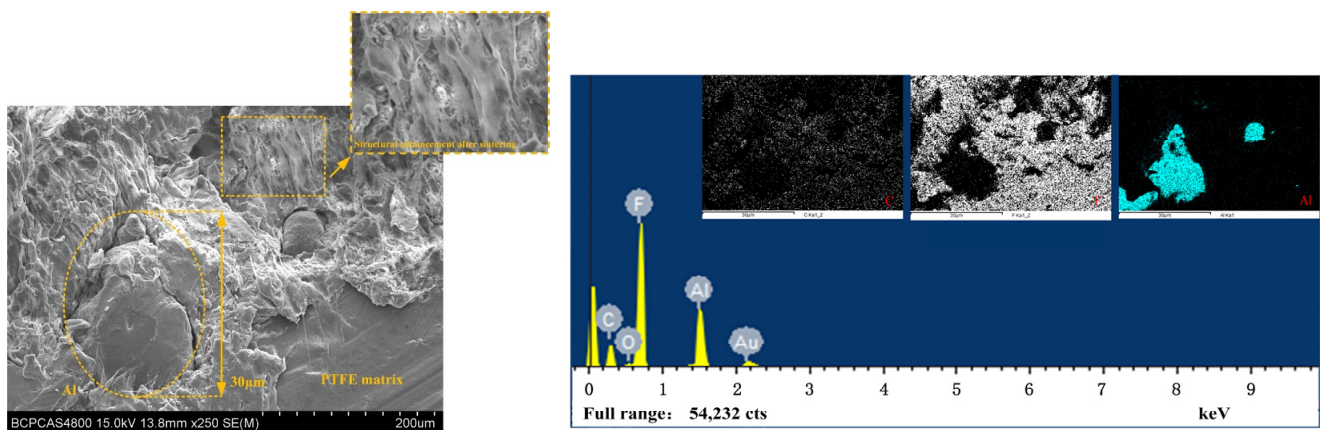


**Figure 3.** SEM and EDS scanning results.

**Table 3.** EDS surface scan elemental analysis results.

Chemical Element	C	O	F	Al	Au
Weight percent (%)	24.02	1.32	59.30	11.12	4.25
Atomic percent (%)	35.48	1.46	55.37	7.31	0.38

## 2.2. Experimental Methods

The experimental reactive liner shaped charges consisted of a reactive liner, the main charge, and a case. Common shapes of the liner included conical, trumpet, and spherical. The cone angle of the shaped charge liners is generally selected from 50° to 80° [28]. For this paper, a conical reactive liner with a cone angle of 60° was selected. The structure of the reactive liner samples and the shaped charge are illustrated in Figure 4. The structure of the shaped charge was a cylinder with a boat tail. The main charge was fabricated by pressing the 8701 explosive with a density of 1.70 g/cm<sup>3</sup>. The material of the case was Steel 1006. The parameters of the shaped charge structure are listed in Table 4, detailing the length of the charge ( $L_c$ ), the charge radius ( $R_{\text{charge}}$ ), the case thickness ( $\delta_{\text{case}}$ ), the liner thickness ( $\delta_{\text{liner}}$ ), the liner step thickness ( $\delta_{\text{step}}$ ), the liner diameter ( $\varnothing_{\text{liner}}$ ), the outer radius of the liner ( $R_{\text{outer}}$ ), the inner radius of the liner ( $R_{\text{inner}}$ ), the cone angle of the liner ( $\theta$ ), and the boat tail angle of the charge ( $\theta_B$ ).

**Table 4.** Structural parameters of reactive liner shaped charge.

$L_c/\text{mm}$	$R_{\text{charge}}/\text{mm}$	$\delta_{\text{case}}/\text{mm}$	$\delta_{\text{liner}}/\text{mm}$	$\delta_{\text{step}}/\text{mm}$	$\varnothing_{\text{liner}}/\text{mm}$	$R_{\text{outer}}/\text{mm}$	$R_{\text{inner}}/\text{mm}$	$\theta/^\circ$	$\theta_B/^\circ$
150	75	5	15	10	150	20	5	60	135

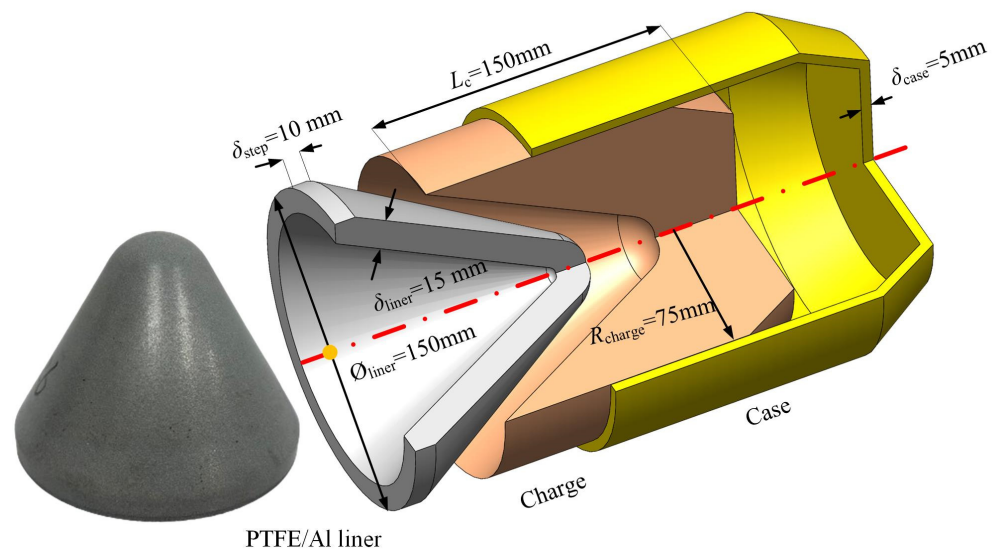


**Figure 4.** Structure of reactive liner shaped charge.

According to research results by Baker [21], the optimal stand-off of the reactive liner shaped charge should be selected as 0.5~1.5 times the charge diameter; 1.0 times the charge diameter was selected as the stand-off in this paper. The experimental principle and setup are depicted in Figure 5, positioning the shaped charge on a stand-off tube at the center of the composite concrete structure, with a stand-off of 150 mm. The shaped charge was detonated at the central point using a detonating device. A total of three experimental groups were conducted, with concrete layer thicknesses set at  $H_c = 250$  mm, 350 mm, and 450 mm, respectively. Additionally, to compare the damage effects of the reactive jets versus the inert jets, a control experiment using an Al liner shaped charge was performed on a  $H_c = 450$  mm composite concrete structure. The Al liner shaped charge was of the same mass as the reactive liners, with all other experimental conditions kept constant. The experimental process was recorded using a high-speed camera (Phantom V 1612, Vision Research, Inc., Wayne, NJ, USA), capturing at a frame rate of 16,000 frames per second and an image resolution of  $1280 \times 800$  pixels.

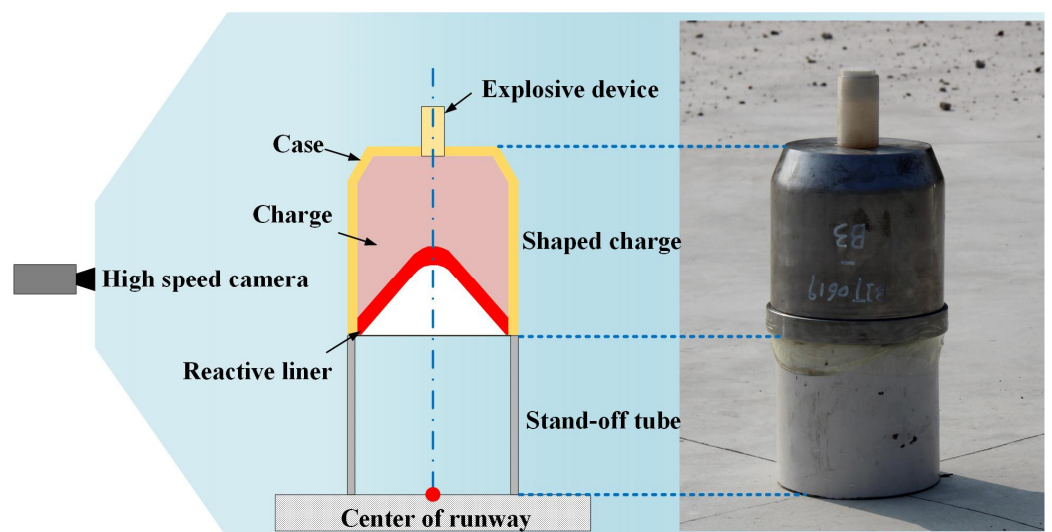


**Figure 5.** Experimental principle and setup.

### 2.3. Numerical Methods

#### 2.3.1. Material Model

To further investigate the causes of dynamic damage in composite concrete structures of varying thicknesses, a numerical simulation study of reactive jet penetration and explosion on composite concrete structures was conducted. The concrete RHT model incorporated three envelope surfaces: the initial yield surface, the failure surface, and the residual strength surface. The effect of the strain rate on yield and damage evolution was also taken into account.

The residual strength surface of the standard RHT model in the principal stress space presented a circular deviated plane, which led to a hardening response rather than the anticipated softening after the peak failure strength was reached. Tu modified the RHT model by simplifying the tension-to-compression meridian ratio,  $\psi$ , in the K&C model and adjusting the dynamic increase factor,  $DIF$ , with the result that the modified RHT model reflected the characteristics of concrete under tensile damage more accurately [29,30].

$$\psi(p) = \begin{cases} 1/2 & p \leq 0 \\ 1/2 + 3f_t/2f_c & p = f_c/3 \\ \alpha f_c / [a_0 + (2\alpha f_c/3)/(a_1 + 2a_2\alpha f_c/3)] & p = 2\alpha f_c/3 \\ 0.753 & p = 3f_c \\ 1.0 & p \geq 8.453f_c \end{cases} \quad (1)$$

$$DIF(\dot{\epsilon}) = \begin{cases} \left(\frac{\dot{\epsilon}}{\dot{\epsilon}_0}\right)^\delta & \text{For } \dot{\epsilon} \leq 1\text{s}^{-1} \\ \beta \left(\frac{\dot{\epsilon}}{\dot{\epsilon}_0}\right)^{1/3} & \text{For } \dot{\epsilon} > 1\text{s}^{-1} \end{cases} \quad (2)$$

where,  $P$  represents pressure and  $f_c$  represents the unconfined compressive strength of the concrete. The detailed explanation and determination of  $\alpha$ ,  $a_0$ ,  $a_1$ , and  $a_2$  within the formula can be found in references [31,32].  $\dot{\epsilon}$  stands for the quasi-static strain rate,  $\dot{\epsilon}_0 = 1 \times 10^{-6}\text{s}^{-1}$ , and  $\delta$  is a constant that correlates to the grade of concrete based on the quasi-static uniaxial compressive strength, defined as  $\delta = 1/(1 + 8f_{cs}/f_{co})$ , where  $f_{co} = 10$  MPa. The coefficient  $\beta$  is a function of  $\delta$ .

Considering the combined penetration–explosion effects on concrete structures, where the primary modes of failure are compressive damage during jet penetration and tensile damage during the explosion, this study utilizes AUTODYN to implement the modified RHT model for describing the dynamic response of concrete layers under jet penetration and explosive loading. Material parameters are detailed in Table 5. The cement-stabilized gravel layer and soil layer materials are derived from reference [33]; the cement-stabilized gravel layer had a compressive strength of 6 MPa.

Before the delay time of the reactive jet,  $\tau$ , the jet was considered inert. The SHOCK equation of state was used, along with the Johnson–Cook strength model, which effectively describes material behavior under large strains, high strain rates, and elevated temperatures. This model posits that the yield strength of the material is influenced by strain, strain rate, and temperature, with stress,  $\sigma$ , determined by:

$$\sigma = [A + B\varepsilon_p^n][1 + C \ln \frac{\dot{\varepsilon}_p}{\dot{\varepsilon}_0}][1 - \left(\frac{T - T_{\text{room}}}{T_{\text{melt}} - T_{\text{room}}}\right)^m] \quad (3)$$

where  $A$ ,  $B$ ,  $C$ ,  $n$ , and  $m$  are material constants,  $\varepsilon_p$  is the effective plastic strain, and  $\dot{\varepsilon}_0 = 1\text{s}^{-1}$  is the plastic strain rate.  $T_{\text{melt}}$  and  $T_{\text{room}}$  represent the melting temperature and the room temperature of the material, respectively. Similarly, steel and aluminum are also described using the SHOCK equation and the Johnson–Cook strength model, with material parameters listed in Table 6. The parameters for the unreacted PTFE/Al

materials were taken from reference [34], while the material data for Steel 1006 and Al 2024 were sourced from the Autodyn material library. In addition, the air material used the ideal gas model, and the material parameters were also sourced from the Autodyn material library.

After the delay time of the reactive jet,  $\tau$ , the jet exploded. Research by Ren et al. [35] showed that the PTFE/Al material reacts violently and can be considered a heterogeneous explosive. The JWL state equation was used to describe the gas products of the PTFE/Al material:

$$P = A_1 \left(1 - \frac{\omega}{R_1 V}\right) e^{-R_1 V} + B_1 \left(1 - \frac{\omega}{R_2 V}\right) e^{-R_2 V} + \frac{\omega E_0}{V} \quad (4)$$

where  $P$  is the pressure;  $V = 1/\rho_e$  is the specific volume;  $\rho_e$  is the density;  $E_0$  is the specific internal energy per unit mass; and  $A_1$ ,  $B_1$ ,  $R_1$ ,  $R_2$ , and  $\omega$  are the material constants. The parameters of PTFE/Al and the 8701 explosive are listed in Table 7.

**Table 5.** Concrete material parameters.

Parameter	Comment	Parameter	Comment
Shear modulus (GPa)	16.3	Elastic strength/ $f_t$	0.7
Compressive strength $f_c$ (MPa)	47.3	Elastic strength/ $f_c$	0.53
Tensile strength $f_t/f_c$	0.108	Residual strength const. $B$	1.8
Shear strength $f_s/f_c$	0.11	Residual strength exp. $M$	0.7
Failure surface parameter A	2	Comp. strain rate exp. $\alpha$	0.032
Failure surface parameter N	0.7	Damage constant $DI$	0.04
Tens./compr. mMeridian ratio	0.6805	Min. strain to failure	0.01
Brittle to ductile transition	0.0105	Residuals hear modulus frac.	0.13
G(elas.)/G(elas-plas.)	2	Erosion strain/instantaneous geometric strain (only for Lagrange)	2

**Table 6.** Material parameters of inert PTFE/Al, steel, and aluminum.

Materials	$\rho$ (g/cm <sup>3</sup> )	$G$ (GPa)	$A$ (MPa)	$B$ (MPa)	$N$	$C$	$m$	$T_{melt}$ (K)	$C_a$ (km/s)	$S_1$	$\Gamma$
Steel 1006	7.83	77	507	320	0.28	0.064	1.06	1793	4.57	1.92	2.17
PTFE/Al	2.27	0.666	8.044	250.6	1.8	0.4	1.0	500	1.45	2.2584	0.9
Al 2024	2.74	22.7	250	225	0.37	0.067	1.0	775	5.33	1.34	2.0

**Table 7.** Material parameters of the 8701 explosive and PTFE/Al after reactivation.

Materials	$\rho_0$ (g/cm <sup>3</sup> )	$D$ (km/s)	$P_{c_j}$ (GPa)	$A_1$ (GPa)	$B_1$ (GPa)	$R_1$	$R_2$	$\omega$
PTFE/Al	2.27	5.2	21	15.9	0.0023	7	0.6	0.38
8701 explosive	1.71	8.315	28.6	524.23	7.678	4.2	1.1	0.34

### 2.3.2. Numerical Model

Numerical modeling is a critical procedure in determining the accuracy of computational results. Current mainstream computational methods primarily include the Lagrange algorithm, the Euler algorithm, the ALE (Arbitrary Lagrangian Eulerian) algorithm, the CEL (Coupled Eulerian–Lagrangian) algorithm, and the FEM-SPH (Finite Element Method–Smoothed Particle Hydrodynamics) coupling algorithm. Each of these methods has its advantages, considering the specific requirements of the simulation. The Euler algorithm is frequently used in simulating fluids, gases, and large deformation problems, such as jet formation from shaped charges. The FEM-SPH algorithm is particularly effective for calculating jet or projectile penetration in brittle materials, offering a more accurate description of brittle material fracture and large deformation in solids. The challenge of dynamic

damage in composite concrete structures under combined penetration and explosion actions involves complex force–thermal–chemical coupling and deformation and fracture under high dynamic loads. Therefore, different computational methods were employed at various stages to address these challenges, as illustrated in Figure 6.

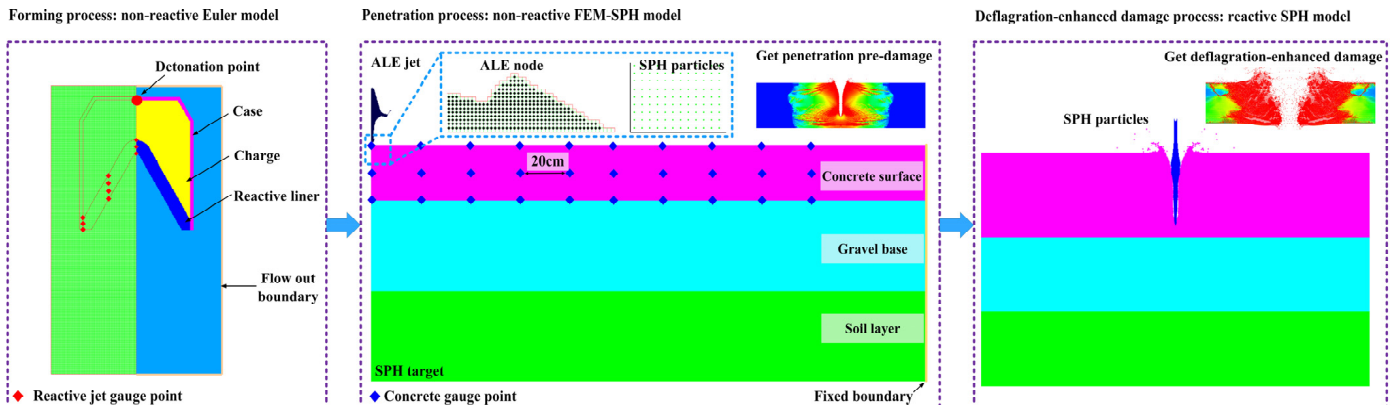


**Figure 6.** Numerical simulation model.

(1) Jet forming stage: the Euler algorithm was used to compute the inert jet formation behavior without reactive characteristics. For the forming stage, the flow-out boundary conditions were set at the Euler grid boundary.

(2) Kinetic penetration stage: the Euler jet was mapped to an ALE jet, and the composite concrete structure target was modeled using SPH particles. The FEM-SPH algorithm was then applied to calculate the damage caused by kinetic penetration.

(3) Explosion-enhanced stage: a post-processing development was used to convert the ALE jet into SPH particles with reactive parameters. A restart mechanism was employed to compute the explosion-enhanced damage. For the penetration and explosion stage, fixed boundary conditions were set at the boundaries of the composite concrete structure.

The entire computational process utilized an Autodyn-2D axisymmetric model. The Euler grid size during the forming process was  $1\text{ mm} \times 1\text{ mm}$ , the ALE jet grid size during penetration was  $1\text{ mm} \times 1\text{ mm}$ , and the target SPH particle size was  $2\text{ mm}$ . Each part of the model interacted with the other parts through the interaction settings of AUTODYN 18.2.

### 2.3.3. Grid Convergence Analysis

To ensure computational accuracy while minimizing the grid size, a comprehensive grid convergence analysis was conducted. During the formation stage, grid sizes of  $0.5\text{ mm} \times 0.5\text{ mm}$ ,  $1\text{ mm} \times 1\text{ mm}$ ,  $2\text{ mm} \times 2\text{ mm}$ , and  $5\text{ mm} \times 5\text{ mm}$  were evaluated, with the velocity of the jet tip over time illustrated in Figure 7a. It was observed that, with a grid size of  $5\text{ mm} \times 5\text{ mm}$ , a significant distortion in the jet tip velocity occurred, indicating a loss of detail and precision. To further refine the analysis, target particle sizes of  $1\text{ mm}$ ,  $2\text{ mm}$ ,  $4\text{ mm}$ , and  $8\text{ mm}$  were compared, alongside velocity changes of the jet head during penetration. This comparison was benchmarked against the CEL method using a  $2\text{ mm} \times 2\text{ mm}$  grid. The findings revealed that grid sizes smaller than  $2\text{ mm}$  exhibited good convergence, suggesting a balanced approach between computational efficiency and accuracy. Based on these results, the grid sizes specified in Section 2.3.2. were deemed appropriate for the ensuing computations, ensuring both precision and practicality in the numerical simulations.

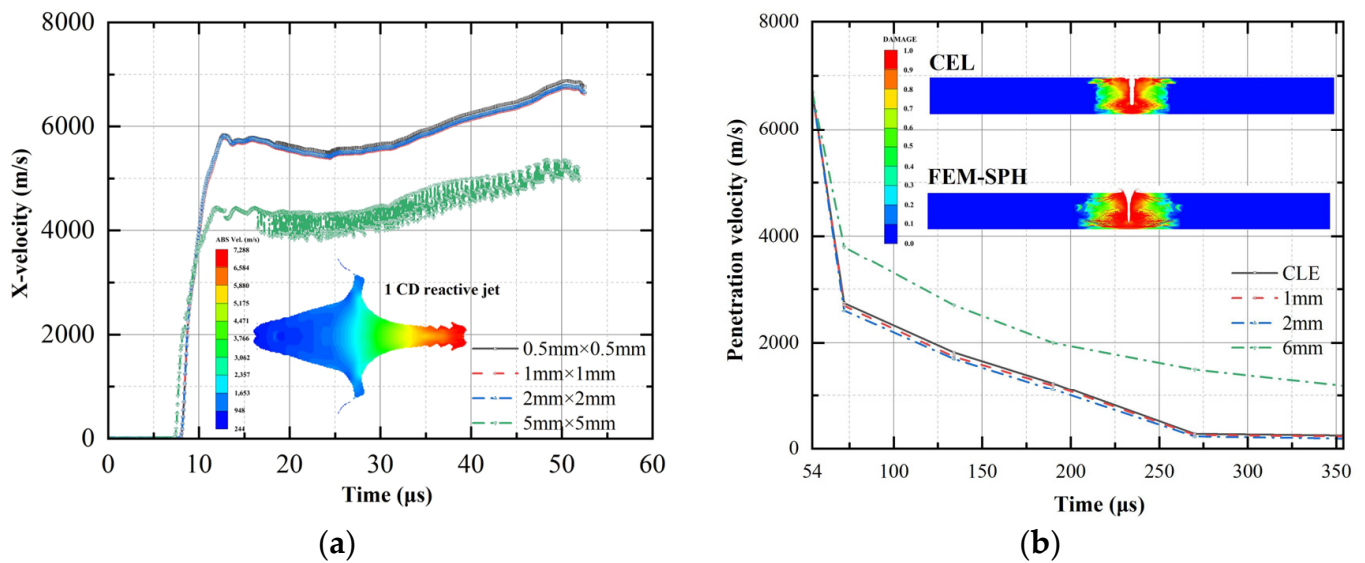


**Figure 7.** Analysis of grid convergence: (a) Variation of the jet tip velocity with time, (b) jet penetration velocity with time.

### 3. Results and Discussion

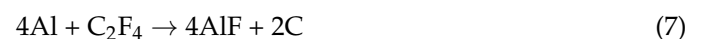
#### 3.1. Experimental Results

##### 3.1.1. Dynamic Damage Results in Composite Concrete Structures

High-speed photography captured the dynamic damage process to composite concrete structures by reactive jets, as illustrated in Figure 8. At  $t = 0 \mu\text{s}$ , the charge detonated; by  $t = 312.5 \mu\text{s}$ , the charge emitted a bright flare; at  $t = 375 \mu\text{s}$ , black products appeared within the flare due to the impact-induced thermal effect, which caused the internal matrix of the reactive jet to disintegrate and release the gas product,  $\text{C}_2\text{F}_4$ , with strong oxidation:



The decomposition of the matrix and the exothermic reaction with aluminum powder proceeded as follows:



Formulas (6) through (8) suggest that, after the reaction of the reactive jet, a significant amount of solid carbon (C) was produced, signifying that an explosive reaction occurred in the penetration hole. By  $t = 30 \text{ ms}$ , the carbon dispersed with the smoke, and fragments of the damaged concrete layer and base material were ejected.

The structure damage results of the composite concrete structure with  $H_c = 250 \text{ mm}$  are shown in Figure 9. A central penetration hole and surrounding funnel crater were formed. Radial cracks radiating towards the boundary appeared in the concrete layer, along with fine circumferential cracks. Observed from a horizontal perspective, a significant bulge was apparent, which showed the highest position at the center and the lowest position at the edge. The diameter of the central penetration hole ( $D_p$ ) was 37 cm. The diameter of the funnel crater ( $D_c$ ) was 87 cm × 75 cm. The diameter of the circumferential cracks ( $R_c$ ) was 330 cm. The number of radial cracks ( $L$ ) was eight. The bulge height ( $\delta_b$ ) at the center of the target, measured with a triaxial level, was 6 cm.

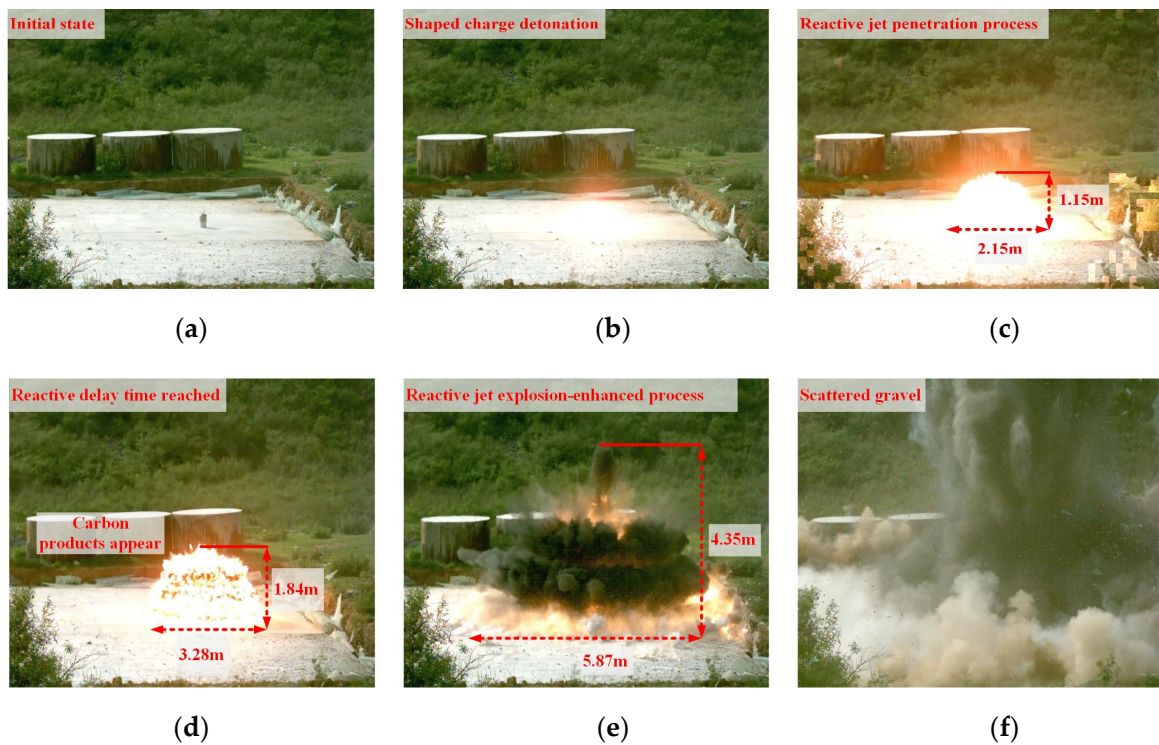


**Figure 8.** High-speed photographic capture of the dynamic damage process to composite concrete structures by reactive jets: (a) Initial state, (b)  $t = 0 \mu\text{s}$ , (c)  $t = 312.5 \mu\text{s}$ , (d)  $t = 375 \mu\text{s}$ , (e)  $t = 812.5 \mu\text{s}$ , (f)  $t = 30 \text{ ms}$ .

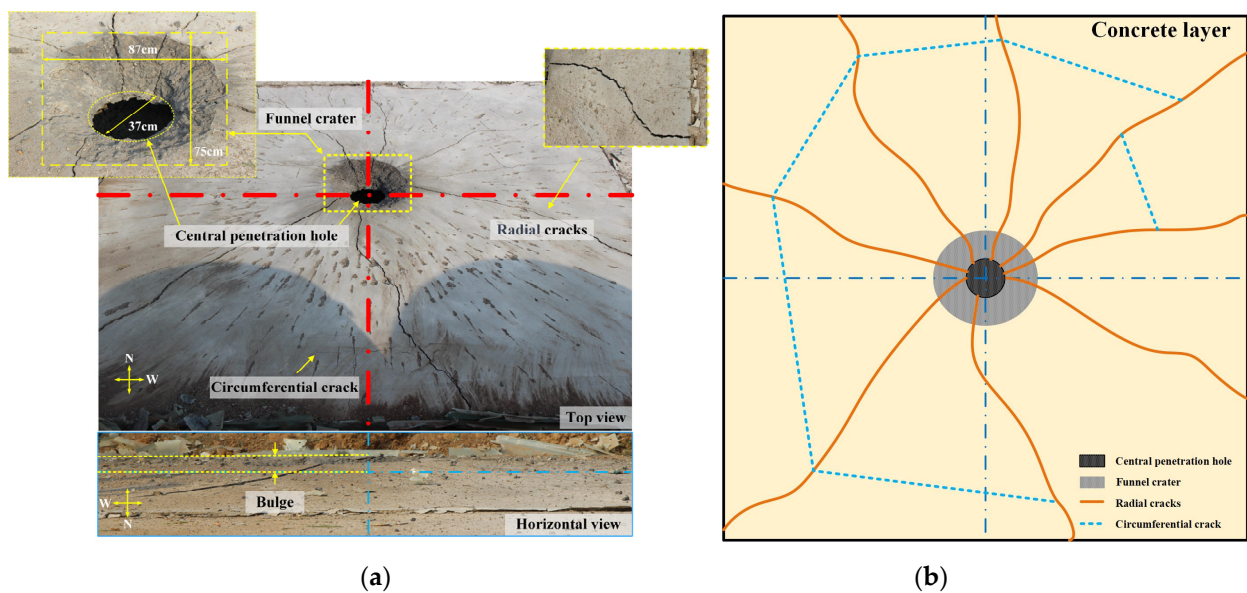


**Figure 9.** Dynamic damage results of the  $H_c = 250 \text{ mm}$  composite concrete structure due to reactive jet impact: (a) Experimental results, (b) Damage diagram.

### 3.1.2. Influence of Concrete Layer Thickness

Experiments were conducted on composite concrete structures with thicknesses of  $H_c = 350 \text{ mm}$  and  $H_c = 450 \text{ mm}$ , under identical experimental conditions, with the results presented in Figure 10. The results indicated that, for an  $H_c = 350 \text{ mm}$  thickness, the concrete layer exhibited seven radial cracks penetrating through, with the  $D_c$  measuring  $97 \text{ cm} \times 105 \text{ cm}$ , and  $\delta_b = 3 \text{ cm}$ . When the thickness was increased to  $H_c = 450 \text{ mm}$ , the concrete layer developed four radial cracks, with the  $D_c$  expanding to  $198 \text{ cm} \times 160 \text{ cm}$ ; no

observable bulge was noted. Comparing Figures 9 and 10 revealed that, as the thickness of the concrete layer increased, the  $D_c$  gradually enlarged yet the  $L$  and the  $\delta_b$  tended to decrease.

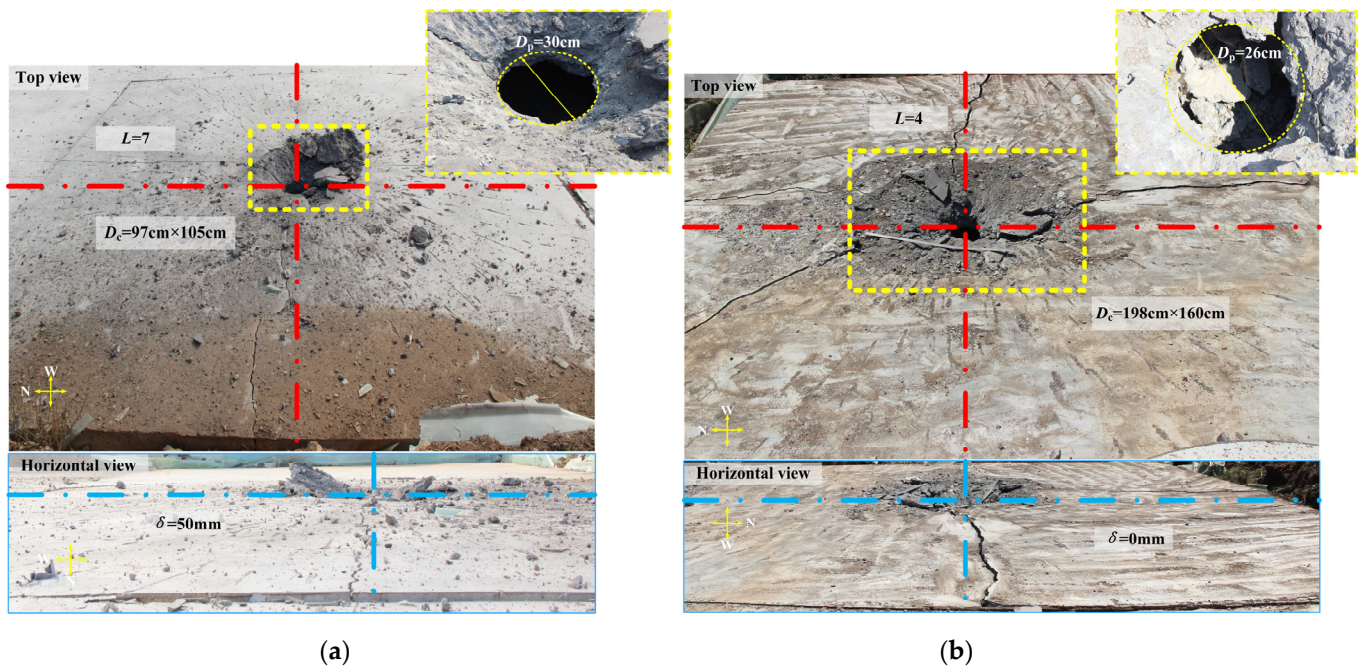


**Figure 10.** Dynamic damage results in composite concrete structures at different thicknesses: (a)  $H_c = 350$  mm, (b)  $H_c = 450$  mm.

### 3.1.3. Comparison of PTFE/Al Jet and Al Jet Damage

An experiment was conducted using an Al liner to damage a composite concrete structure with  $H_c = 450$  mm thickness under identical experimental conditions. Since the Al jet was an inert jet, no explosion reaction occurred during the penetration process. In order to make a more intuitive damage comparison and save costs, the experiment was continued on an intact portion of the composite concrete structure, where the  $H_c = 450$  mm experiment with the reactive jet was conducted. It is noteworthy that, although the Al jet experiment was conducted on an intact portion of the composite concrete structure, this structure had already sustained damage during previous experiments. Moreover, the Al jet test was conducted closer to the boundary, which might have introduced a stronger boundary effect reflection gain. However, the damage resulting from the Al jet was still significantly less than that caused by reactive jets under the same conditions, aligning with the findings by Baker et al. [21].

The dynamic damage process of the Al jet impacting the composite concrete structure is depicted in Figure 11. At  $t = 250 \mu\text{s}$ , the detonation profile of the charge was essentially identical to that shown in Figure 8c. By  $t = 812.5 \mu\text{s}$ , compared with Figure 8d, the illumination from the charge remained bright and unobscured by black products. At  $t = 1250 \mu\text{s}$ , the glow of the detonation hovered in the air, surrounded by visible white detonation products, attributable to the 8701 charge primarily consisting of an RDX explosive. The detonation equation for the charge, as indicated by Equation (9), primarily produced gaseous  $\text{N}_2$ ,  $\text{CO}$ , and  $\text{H}_2\text{O}$  as products. Therefore, by integrating the damage processes of both the reactive and Al jets, it can be concluded that, for the charge conditions presented in this study, the reaction delay time of the reactive materials should be between  $312.5 \mu\text{s}$  and  $375 \mu\text{s}$ . To facilitate the subsequent analysis, the average value of  $\tau = 344 \mu\text{s}$  was taken as the reaction delay time.



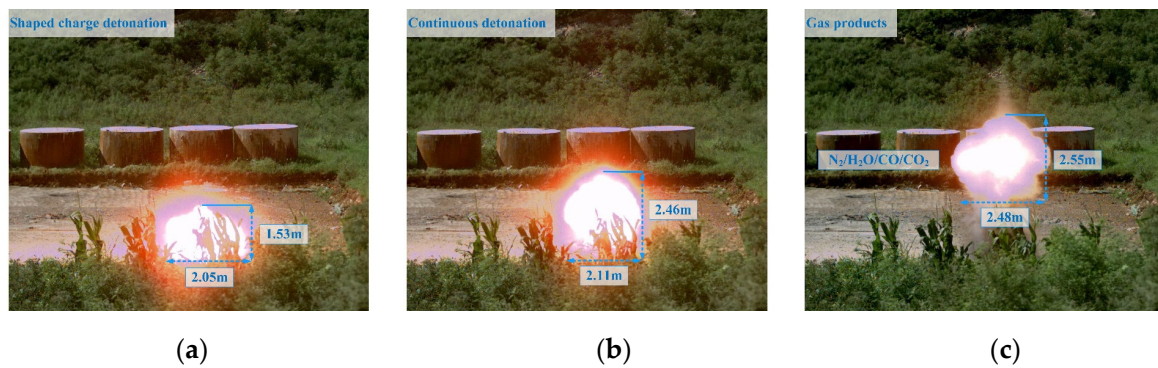


**Figure 11.** High-speed photographic capture of the dynamic damage process to composite concrete structures by Al jet: (a)  $t = 312.5 \mu\text{s}$ , (b)  $t = 812.5 \mu\text{s}$ , (c)  $t = 1250 \mu\text{s}$ .

The comparison of damage between the reactive and Al jets, alongside the specific details of the Al jet damage, are illustrated in Figure 12. The  $D_c$  caused by the Al jet amounted to 21.4% of that caused under similar conditions by the reactive jet; the  $D_p$  is 56.5% of the reactive jet under the same conditions. Additionally, radial cracks at the edge of the penetration hole were notably finer and shorter in extent when caused by the Al jet. The dynamic damage results of the composite concrete structure are summarized in Table 8.

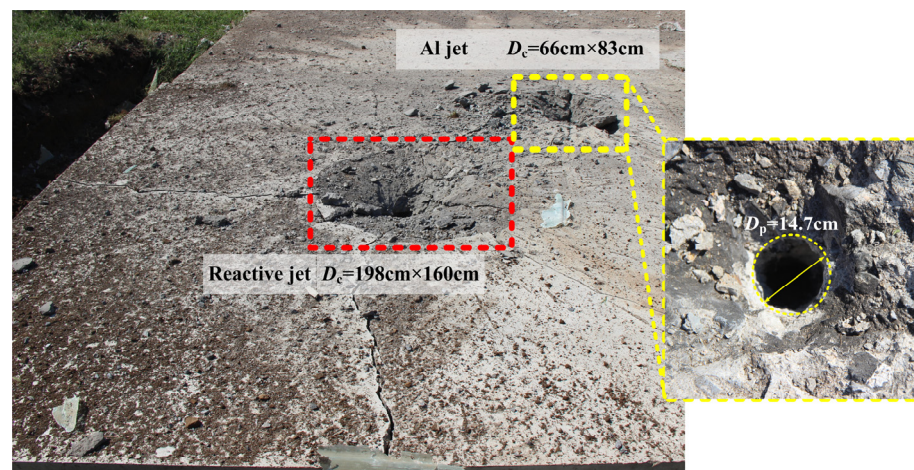


**Figure 12.** Comparison of composite concrete damage affected by the Al jet and the reactive jet.

**Table 8.** Comparison of dynamic damage results of composite concrete structures.

Number	$H_c$ (cm)	$D_p$ (cm)	$D_c$ (cm)	$\delta_b$ (cm)	$L$	$R_c$ (cm)
Reactive-1	250	37	$87 \times 75$	6	8	330
Reactive-2	350	30	$97 \times 105$	3	7	-
Reactive-3	450	26	$198 \times 160$	0	4	-
Al	450	14.7	$66 \times 83$	0	3	-

### 3.2. Dynamic Response of Composite Concrete Structures to Reactive Jet Penetration

The dynamic response of the composite concrete structures subjected to reactive jet penetration is depicted in Figure 13. During penetration, the concrete at the penetration interface was damaged by jet compression, at the same time, the concrete medium near the axis of symmetry fractured under the combined action of the radial and circumferential tensile stresses, resulting in the formation and expansion of microcracks. Figure 13a illustrates the initial state of the jet penetration and compression wave propagation.

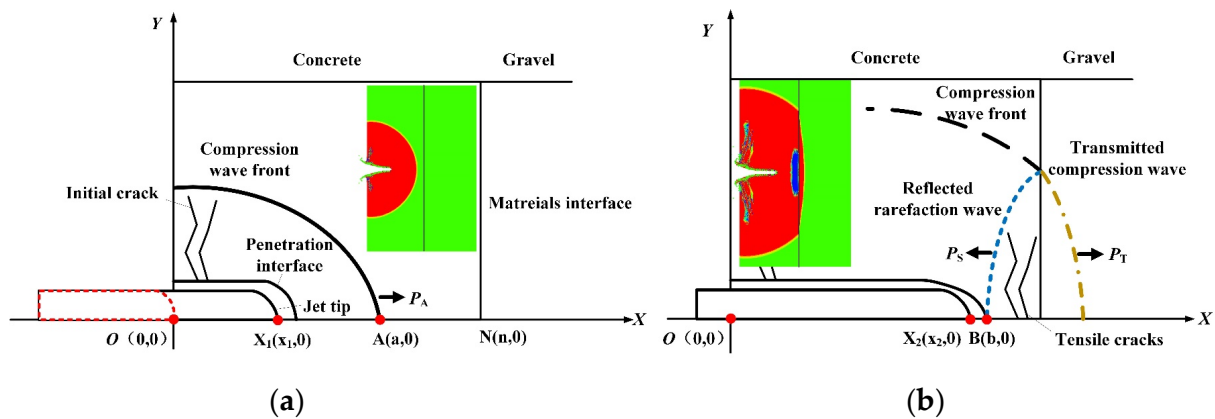


**Figure 13.** Mechanism of dynamic response in composite concrete structures under jet penetration: (a) initial damage; (b) tensile damage.

An initial compression wave was generated by the jet at point  $O$ , causing compressive damage along the axial direction of the concrete material. When the reactive jet penetrated the target, ignoring the internal pressure of the material itself, the pressure at the projectile–target interface was derived using the Bernoulli equation:

$$P_0 = \frac{1}{2} \rho_j (v_j - u_0)^2 = \frac{1}{2} \rho_t u^2 \tag{10}$$

where  $P_0$  represents the initial pressure of the incoming compression wavefront,  $\rho_j$  is the density of the jet material,  $v_j$  is the velocity of the jet tip, and  $u$  is the penetration velocity induced in the target by the impact of the jet.

The initial compression wave exhibited an exponential decay. When it propagated to any point  $A(a,0)$  within the concrete, its intensity decreased to [36]:

$$P_A = P_0 e^{-\gamma a} \tag{11}$$

where  $P_A$  is the pressure of the compression wavefront at point  $A$ ,  $a$  is the distance of the wavefront propagation, and  $\gamma$  is the attenuation coefficient of the target material.

At this point, the stress distribution due to the concentrated load on the concrete layer was tracked as:

$$\begin{cases} \sigma_X = -\frac{3}{2} \frac{P_A}{\pi r^2} \cos^3 \varphi \\ \sigma_Y = \frac{1}{2} \frac{P_A}{\pi r^2} \left[ (1 - 2\mu) \frac{1}{1 + \cos \varphi} - 3 \cos \varphi \sin^2 \varphi \right] \\ \sigma_\theta = \frac{1}{2} \frac{P_A}{\pi r^2} (1 - 2\mu) \left( \cos \varphi \frac{1}{1 + \cos \varphi} \right) \end{cases} \tag{12}$$

where,  $\sigma_X$ ,  $\sigma_Y$ , and  $\sigma_\theta$  represent the axial, radial, and circumferential stresses, respectively.  $r$  is the radial distance,  $\varphi$  is the angle, and  $\mu$  is the Poisson’s ratio of the concrete material.

Near the free surface of the concrete, the radial stress was tensile:

$$\sigma_Y = \frac{1 - 2\mu}{2\pi y^2} P_A \tag{13}$$

where,  $y$  represents the radial distances, respectively. When the radial stress,  $\sigma_Y$ , reached the tensile strength,  $\sigma_t$ , initial cracks started to form.

More intricately, when the compaction wave reached the interface between the concrete and gravel materials, reflection and transmission occurred. This disturbance disrupts the stable penetration stress state within the target, as illustrated in Figure 13b. Given that the wave impedance of concrete,  $\rho_c C_c$ , exceeded that of the gravel material,  $\rho_g C_g$ , effectively transitioning from a “hard” to a “soft” material, the arrival of the compression

wave at the interface generated reflected tensile rarefaction waves within the concrete layer. These waves exerted a negative pressure,  $P_s$ , which was directly proportional to the intensity of  $P_A$ . When the tensile pressure,  $P_s$ , surpassed the tensile strength,  $\sigma_t$ , the back side of the concrete experienced tensile fracturing, creating tensile cracks. The dynamic response process of the composite concrete structure under penetration is depicted in Figure 14.

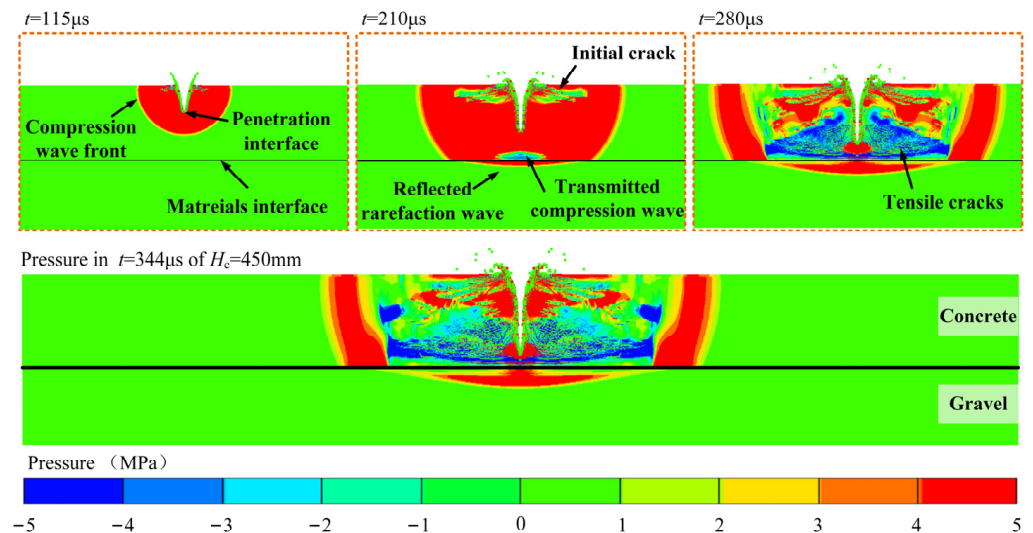


**Figure 14.** Dynamic response process of composite concrete structure under penetration ( $H_c = 450\text{ mm}$ ).

The dynamic damage results of the composite concrete structure under penetration are shown in Figure 15. Initially, the concrete layer developed a central penetration hole due to the high-pressure penetration of the jet, leading to compressive damage around the edge of the hole. Subsequently, initial cracks appeared on the front side of the layer, and the back side of the concrete layer developed tensile cracks, caused by the reflected tensile waves.

During the penetration process, the pressure changes at the gauge points that were 20 cm from the penetration center within the concrete are illustrated in Figure 16. Initially, the concrete was subjected to the penetration of the jet, causing an immediate increase in the internal pressure and compressive damage. Following this, the pressure decreased under the effect of the reflected rarefaction waves. When the pressure dropped below  $\sigma_t$ , the concrete went through tensile damage. Subsequently, the pressure within the target fluctuated under the combined action of penetration compression and reflected tension.

Upon reaching the reaction delay time,  $\tau$ , the penetration depth of the reactive jet is shown in Figure 17, and the damage results of the concrete layer are presented in Figure 18. At the reaction delay time,  $\tau$ , as the thickness of the concrete layer increased, the length of tensile cracks on the back side and the diameter of the penetration hole gradually decreased, while the lengths of the initial cracks on the front side remained essentially consistent. According to Equation (13), under identical conditions, the initial cracks on the front side depended solely on the impact pressure,  $P_0$ , hence the consistency in the crack length. Conversely, the lengths of the cracks on the back side correlated with the tensile pressure,  $P_s$ . As the thickness of the concrete layer increased, it took longer for the compression wave to reach the reflective interface. Within the same reaction time, the shorter duration of action by the reflective pressure,  $P_s$ , resulted in lesser tensile damage on the back side, leading to shorter crack lengths.

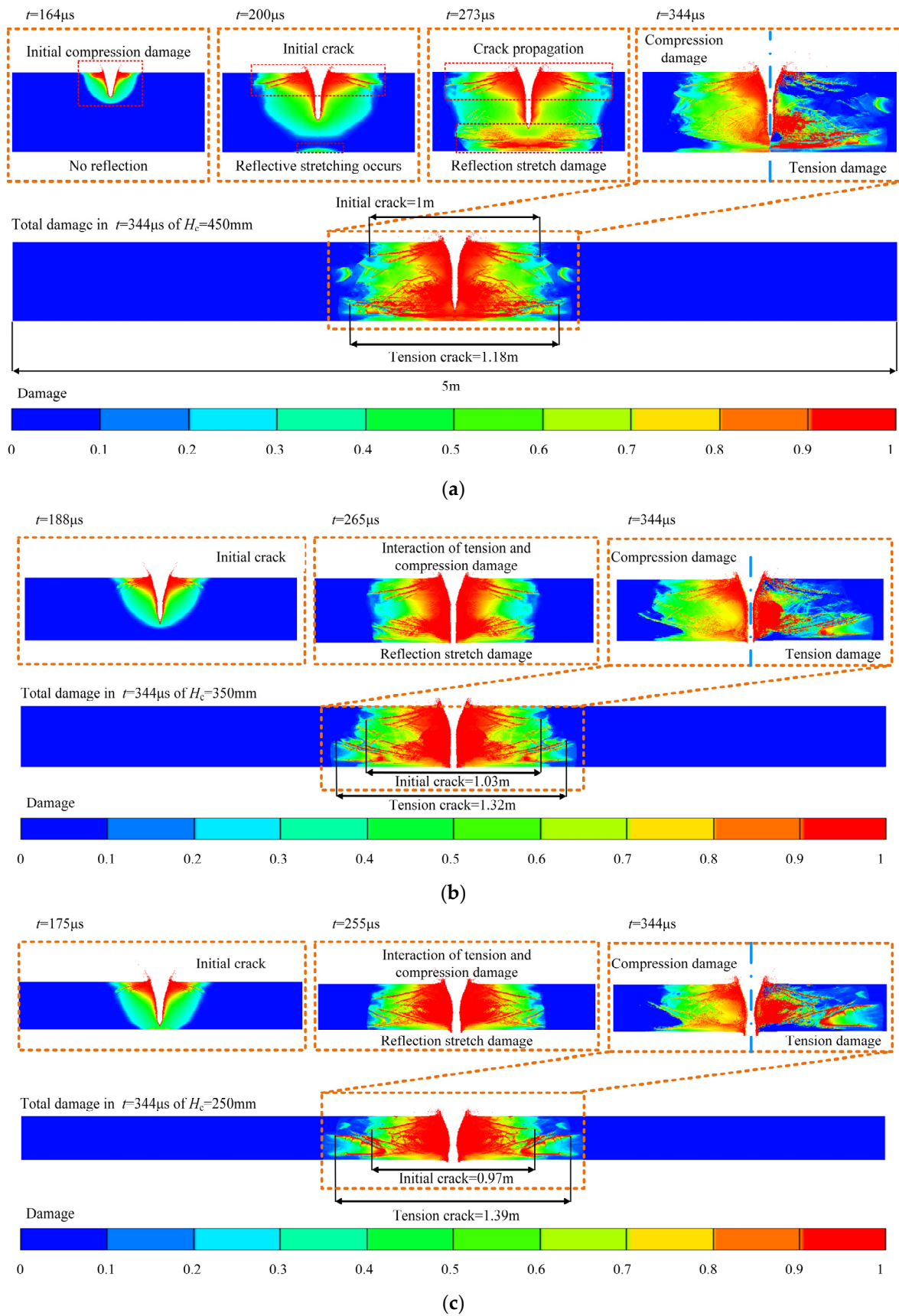


**Figure 15.** Damage results of composite concrete structure under reactive jet penetration: (a)  $H_c = 450$  mm; (b)  $H_c = 350$  mm; (c)  $H_c = 250$  mm.

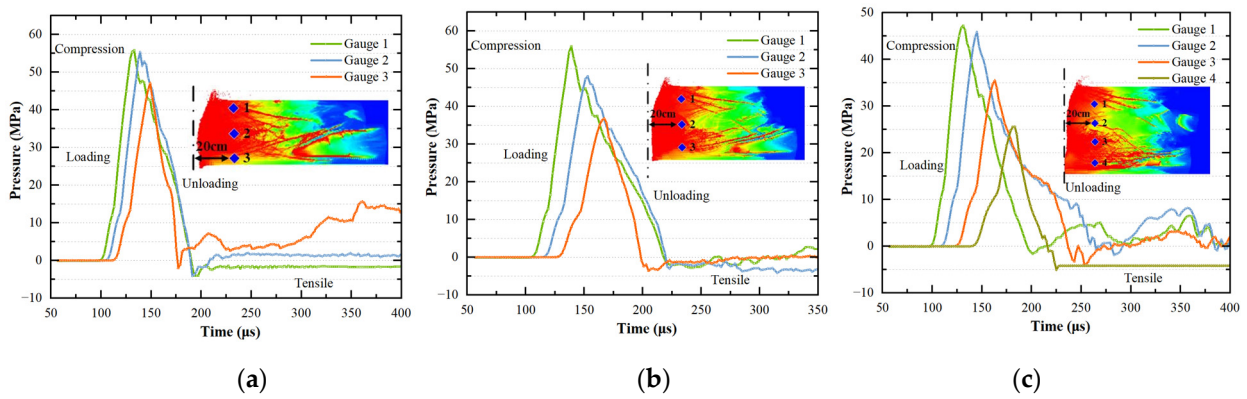


Figure 16. Pressure changes within the concrete layer over time: (a)  $H_c = 250$  mm; (b)  $H_c = 350$  mm; (c)  $H_c = 450$  mm.

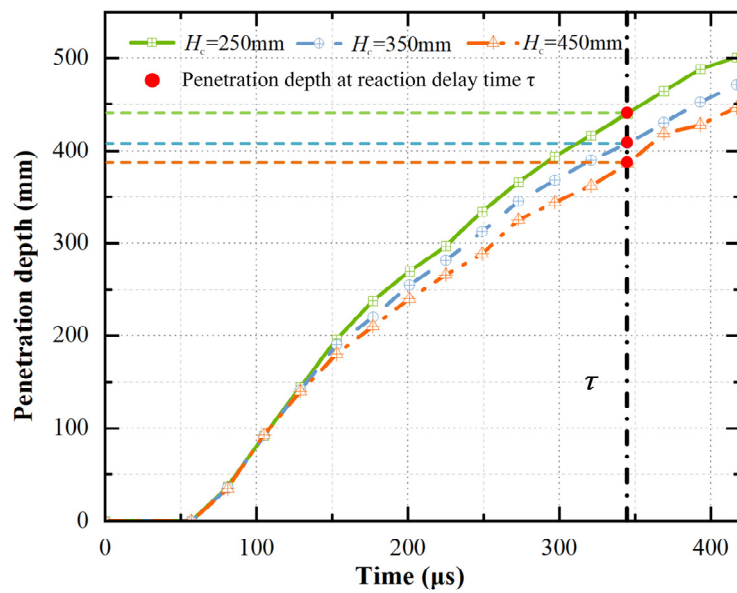


Figure 17. Variation of Penetration Depth Over Time.

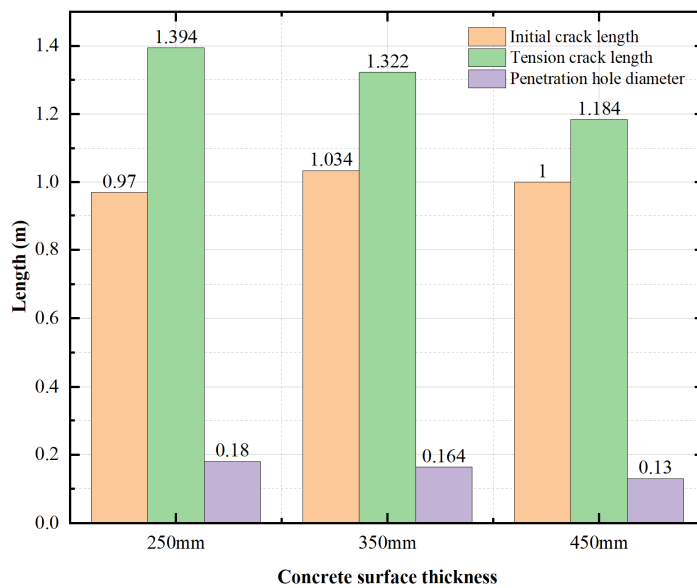


Figure 18. Damage results of the concrete layer at time  $\tau$ .

### 3.3. Explosion-Enhanced Damage Analysis

At the moment  $\tau$ , when the reactive jet underwent an explosive reaction, the material model employed the JWL parameters for PTFE/Al, as listed in Table 7. The mass of the reactive materials was determined based on the mass of the reactive jet. Given that the tip of the jet is a high-temperature, high-pressure zone during penetration, it was assumed that the tip of the reactive jet reacts first. As shown in Figure 17, at the moment  $\tau$ , varying thicknesses led to different penetration depths. The spatial distribution of the reactive jet is depicted in Figure 19, with the mass fraction distribution of the reactive materials provided in Table 9. The varying thicknesses of the concrete layers led to differences in the jet penetration depths, subsequently resulting in different spatial mass distributions of the reactive materials, which is one of the fundamental reasons for the variation in the damage results.

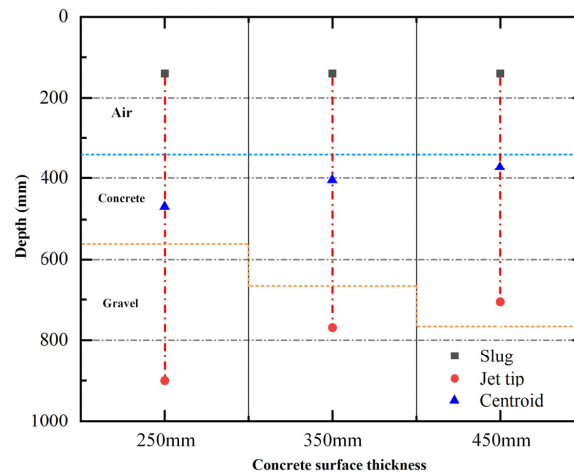


Figure 19. Spatial distribution of the reactive jet at  $\tau$ .

Table 9. Spatial distribution of the mass fractions of the reactive materials.

$H_c$	Initial Mass	Remaining Mass	Mass in Air	Mass in Concrete	Mass in Gravel
250 mm	1057 g	956.5 g	20.7%	37.9%	41.4%
350 mm		964.0 g	31%	54.5%	14.5%
450 mm		983.0 g	37.8%	62.2%	0

For  $H_c = 250$  mm and  $H_c = 350$  mm, the damage can be divided into two parts: (1) within the concrete layer, the mass  $m_1$  of the reactive material caused a compressive expansion effect upon explosion. The explosive shock pressure,  $P_1$ , exerted radial pressure on the concrete layer, leading to partial crushing zones. The diameter of the central penetration hole increased and fragmented concrete was ejected. Eventually, a funnel crater was formed. Additionally, the propagation of the compression waves in the concrete during penetration caused fine radial cracks to extend further due to circumferential stress, forming radiating radial cracks. The width and number of these cracks were directly related to the magnitude of the circumferential stress. (2) In the cement stabilized gravel layer, the mass,  $m_2$ , of the reactive material exploded and produced an expansion effect. At this juncture, the explosive shock pressure,  $P_2$ , generated an upward axial pressure on the concrete layer, leading to the formation of the bulge in the concrete layer. When the stress at the focus of dynamic load exceeded the tensile strength of the concrete layer, the layer fractured, forming circumferential cracks.

For the  $H_c = 450$  mm composite concrete structure, only the first part of the damage occurred, with no second part. The pressures,  $P_1$  and  $P_2$ , can be determined using the following formula [20]:

$$P_{1,2} = m_{1,2} \times \left( 4.7356 \times 105e^{-50.467V} + 30.62e^{-4.9234V} + 0.31403Cv \frac{T}{V} \right) \quad (14)$$

where  $C_v$  is the specific heat capacity at the constant volume of the reactive material, and  $m_1$  and  $m_2$  are the masses of the reactive material in the concrete and gravel layers, respectively.

After 2000  $\mu$ s of the explosion of the reactive materials, the dynamic damage results of the concrete layer under the explosion-enhanced effect are shown in Figure 20. To clearly observe the funnel crater of the concrete, the image was processed for enhanced clarity through grayscale adjustment. Compared with penetration damage, the explosion enhancement led to an expansion effect in the central penetration hole, enlarging the hole diameter. Concrete near the explosion center developed cracks. Over time, the fragmented concrete materials were ejected, forming the funnel craters observed in the experimental results.

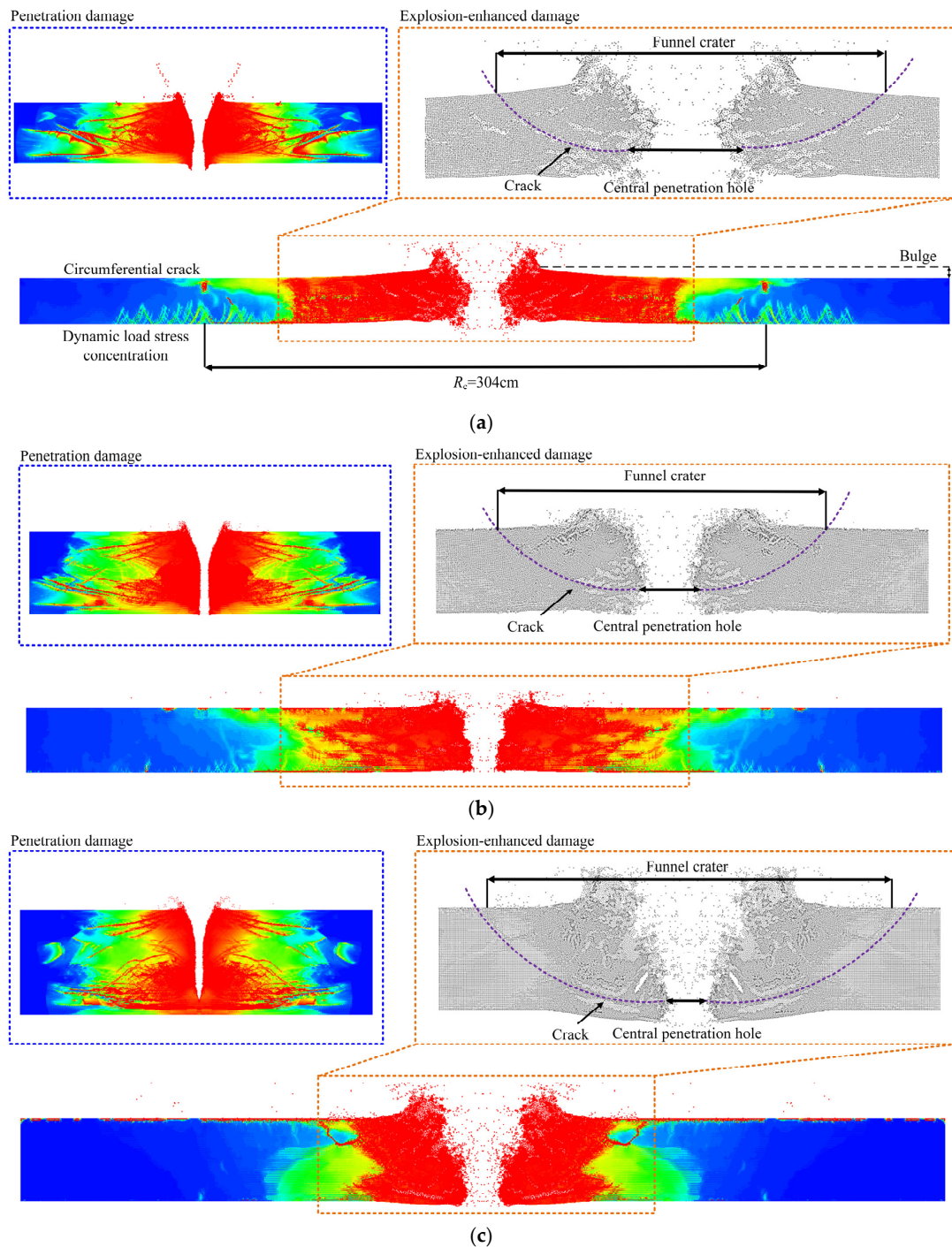


**Figure 20.** Numerical simulation results of explosion-enhanced damage: (a)  $H_c = 250$  mm, (b)  $H_c = 350$  mm, (c)  $H_c = 450$  mm.

According to reference [37], the  $\delta_b$  of the concrete layer under the effect of an internal explosion can be expressed as:

$$\delta_b = A \frac{\bar{P} \times \bar{\Delta t}}{\rho h} \quad (15)$$

where  $A$  is a constant,  $\bar{P}$  represents the average load pressure,  $\bar{\Delta t}$  is the effective duration of the load,  $\rho$  is the density of the concrete layer, and  $h$  is the thickness of the concrete layer.

From Equations (14) and (15), it is evident that the  $\delta_b$  was directly proportional to the mass of the reactive material and inversely proportional to the thickness of the concrete layer. This correlation was consistent with the results from the numerical simulations. As shown in Figure 20a, a noticeable bulge and bending damage occurred in the 250 mm concrete layer, with the experimental circumferential crack diameter  $R_c = 330$  cm, while the numerical simulation showed a stress-concentration diameter of  $R_c = 304$  cm, aligning closely with the experimental values. Figure 20c indicates that the 450 mm concrete layer exhibited almost no bulge. The axial velocity changed over time at the center of the concrete layer, as shown in Figure 21, revealing that both the 250 mm and 350 mm concrete layers experienced a significant step-like negative axial velocity gradient from the explosion center to the edges, leading to a bulge formation that was higher in the center and lower on the sides. Furthermore, the velocity gradient in the 250 mm concrete layer was larger than that in the 350 mm layer, resulting in a more pronounced bulge. Conversely, the 450 mm concrete layer showed almost no negative axial velocity, hence no bulge formation occurred.

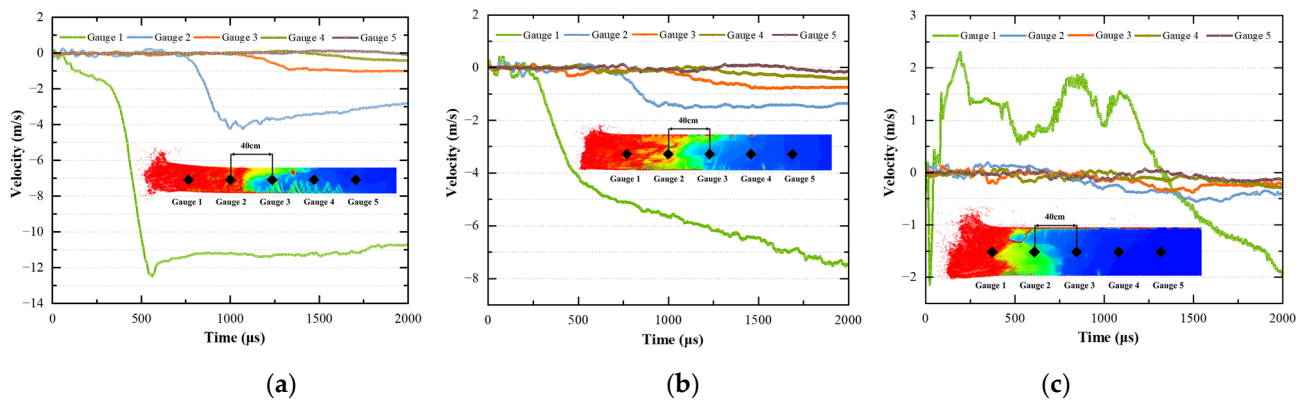


**Figure 21.** Changes in internal pressure within the concrete layer over time for different thicknesses: (a)  $H_c = 250$  mm, (b)  $H_c = 350$  mm, (c)  $H_c = 450$  mm.

The comparison between the numerical simulation results and the experimental results is shown in Figure 22, and the error values are shown in Table 10. It was indicated that the maximum error for the  $D_p$  is 13.3%, and for the  $D_c$  is 12.9%. By taking the numerical simulation results from Figure 20, the diameter of the damage zone where Damage = 1 was  $R_{\text{damage}}$ . The comparison of the penetration hole diameters  $D_p$  and the damage zone diameters  $R_{\text{damage}}$  between the numerical simulations of the reactive jet penetration and explosion-enhanced damage, as depicted in Figure 23, showed that under the dynamic damage from explosion enhancement, the central penetration diameter  $D_p$  increased by an average of 116% and the damage zone diameter  $R_{\text{damage}}$  increased by an average of 59.7%.

**Table 10.** Error table between the numerical simulation results and the experimental results.

$H_c$	Simulation $D_p$ (mm)	Experiment $D_p$ (mm)	Error (%)	Simulation $D_c$ (mm)	Experiment $D_c$ Average Value (mm)	Error (%)
250 mm	41	37	9.8	91	81	11.0
350 mm	31	30	3.3	116	101	12.9
450 mm	30	26	13.3	184	179	2.7

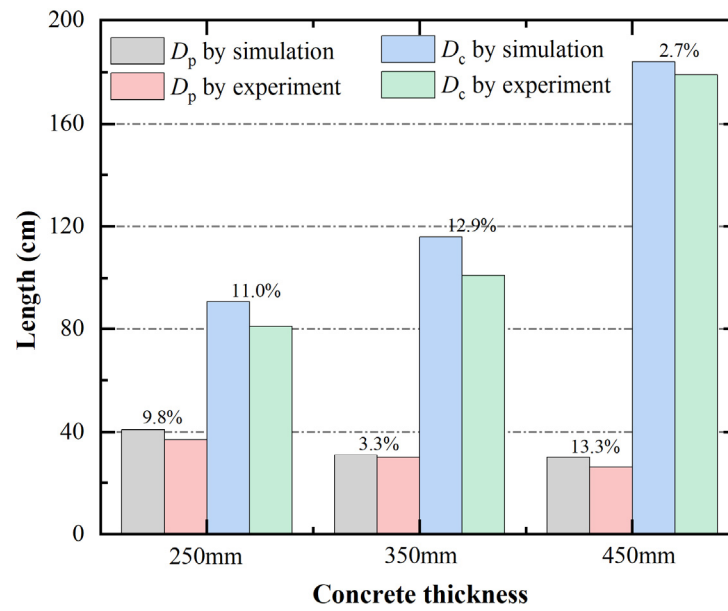


Figure 22. Comparison between the numerical simulation results and the experimental results.

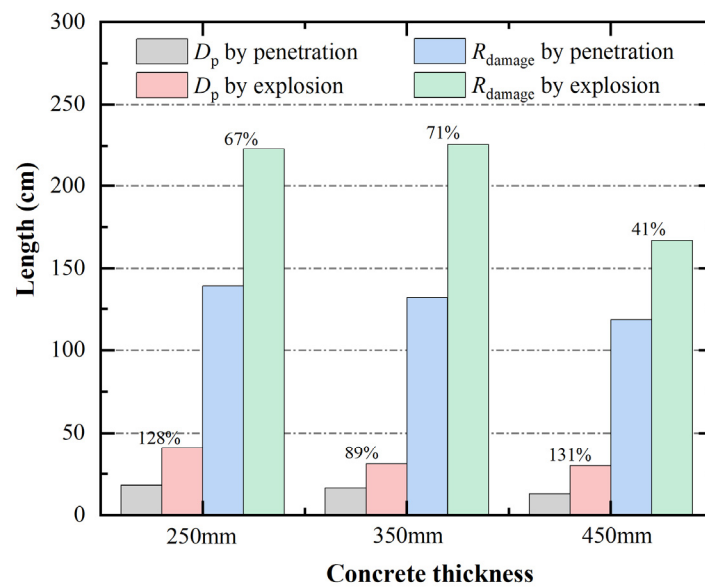


Figure 23. Comparison of damage from the reactive jet penetration and explosion enhancement.

Based on the mechanism analysis, the dynamic damage process of composite concrete structures under the combined action of reactive jet penetration and explosion enhancement mainly includes three stages: jet formation, kinetic energy penetration damage, and explosion-enhanced damage.

(1) Jet formation stage: Under the detonation impact of the shaped charge, the reactive liner collapses and collides along its axis, forming a high-speed jet. This stage initiates the penetration process by concentrating the energy into a focused stream, capable of penetrating the target material at high velocities.

(2) Kinetic energy penetration stage: Before the time reaches  $\tau$ , the reactive jet is considered to be in an inert state. Utilizing its kinetic energy, the high-speed jet penetrates the composite concrete structure, creating a central penetration hole. During this stage, the concrete layer experiences both compressive shock waves, initiated by the jet penetration, and tensile rarefaction waves reflected from the rear, leading to the formation of pre-damage cracks.

(3) Explosion-enhanced damage stage: After the time reaches  $\tau$ , the reactive jet undergoes an explosive reaction, releasing chemical energy and generating shock waves that propagate outward, along with a significant volume of gas products. Under the combined dynamic load of the shock wave and the explosive products, the central penetration hole enlarges, causing fragmentation and a funnel crater in the concrete layer. Simultaneously, circumferential tensile stresses within the concrete layer further extend pre-damage cracks into radial cracks. In the thinner concrete layers, the jet penetrates through to the gravel layer, and the concrete layer rises from the center to the edges under the explosive action. If the concentrated stress exceeds the flexural strength of the concrete, the concrete breaks at the stress concentration points, forming circumferential cracks. For thicker concrete layers, the reactive jet is unable to reach the gravel layer, resulting only in explosive expansion of the penetration hole and the funnel crater without any bulge in the concrete layer.

#### 4. Conclusions

By integrating full-scale damage experiments with numerical simulations, this study conducted an analysis of the dynamic response characteristics of composite concrete structures under the action of reactive jets. This paper systematically investigated the damage behavior of composite concrete structures with varying thicknesses under the combined effects of kinetic penetration and explosion enhancement by PTFE/Al reactive jets, and compared it with the damage caused by Al jets. Numerical simulations of composite concrete structures under the impact of reactive jets were performed, employing a modified RHT model that more accurately depicted the tensile failure of concrete. This model incorporated the reaction delay time of reactive materials to segmentally simulate the dynamic damage behavior of the concrete layer under both kinetic penetration and explosion-enhanced effects. The conclusions are as follows:

(1) Experimental results have unveiled various damage modes in composite concrete structures subjected to the combined penetration and explosion actions of PTFE/Al reactive jets. These damage modes included central penetration holes, funnel craters, bulges, and radial/circumferential cracks. Compared with the damage incurred through the kinetic penetration of Al jets, the combined penetration–explosion action markedly increased the destructiveness to the concrete layer, with the penetration hole diameter increasing by 76.9% and the funnel crater area increasing by 578%.

(2) Numerical simulation results further validated the dynamic damage behavior of the composite concrete structures, revealing the coupling response mechanism of compressive and tensile stresses during penetration with mechanical analysis and the mechanism of dynamic damage formation under explosion enhancement. The use of a modified RHT model and the FEM-SPH algorithm resulted in simulation outcomes that were closely aligned with the experimental data, confirming the effectiveness and accuracy of the model. Numerical simulations indicated that, under the reaction of the reactive jets, the diameter of the penetration holes and the damage zone under explosive enhancement dynamic damage increased by an average of 116% and 59.7%, respectively, compared with kinetic penetration.

(3) The simulation results revealed the spatiotemporal distribution characteristics of the reactive jets and their contribution to explosion-enhanced damage. The dynamic damage modes of composite concrete structures were closely related to the distribution of the reactive material mass. When the concrete layer was thin, the jet penetrated through the concrete layer into the gravel layer, resulting in a smaller funnel crater but a larger bulge. When the concrete layer was thicker, the jet could not penetrate through the concrete layer. An internal explosion occurred within the concrete, leading to a larger funnel crater but no bulge damage.

This study provides a new perspective for understanding the failure mechanism of the composite concrete structures under the combined action of penetration–explosion, and provides important reference data and a theoretical basis for the anti-damage design of composite concrete structures under dynamic damage by a reactive jet. However, this

study currently only analyzes the impact of concrete layer thickness on reactive jet dynamic damage. Future work requires further research on the effects of a reactive jet on gravel layers and soil layers with different strengths and porosity, to provide a multi-faceted reference for the design of composite concrete structures to resist penetration–explosion dynamic damage.

**Author Contributions:** Article writing and data analysis, C.S.; numerical simulation, P.L.; experiment, J.Z.; English writing, A.L.; data curation, Y.Z.; writing—review and editing, H.W. All authors have read and agreed to the published version of the manuscript.

**Funding:** This research was supported by the National Natural Science Foundation of China (Grant No. 12172052).

**Data Availability Statement:** The data presented in this study are available in the article.

**Conflicts of Interest:** The authors declare no conflicts of interest.

## References

- Shafighfard, T.; Kazemi, F.; Bagherzadeh, F.; Mieloszyk, M.; Yoo, D.Y. Chained machine learning model for predicting load capacity and ductility of steel fiber–reinforced concrete beams. In *Computer-Aided Civil and Infrastructure Engineering*; Wiley: Hoboken, NJ, USA, 2024.
- Ambrosini, R.D.; Luccioni, B.M.; Danesi, R.F.; Riera, J.D.; Rocha, M.M. Size of craters produced by explosive charges on or above the ground surface. *Shock Waves* **2002**, *12*, 69–78. [[CrossRef](#)]
- Gupta, L.; Kumar, R. Laboratory studies to assess the fatigue behavior of bituminous concrete mix. In *Recent Developments in Pavement Design, Modeling and Performance: Proceedings of the 2nd GeoMEast International Congress and Exhibition on Sustainable Civil Infrastructures, Egypt 2018—The Official International Congress of the Soil-Structure Interaction Group in Egypt (SSIGE)*; Springer International Publishing: Cham, Switzerland, 2019; pp. 124–134.
- Tan, Z.; Zhang, W.; Cho, C.; Han, X. Failure mechanisms of concrete slab–soil double-layer structure subjected to underground explosion. *Shock Waves* **2014**, *24*, 545–551. [[CrossRef](#)]
- Malvern, L.E.; Ross, C.A. *Dynamic Response of Concrete and Concrete Structures*; NTIS: Springfield, MA, USA, 1986.
- Mandal, J.; Goel, M.D.; Agarwal, A.K. Surface and buried explosions: An explorative review with recent advances. *Arch. Comput. Methods Eng.* **2021**, *28*, 4815–4835. [[CrossRef](#)]
- Chen, L.-M.; Li, S.-T.; Chen, Y.Q.; Zhu, Q. Influence of Reinforcement Diameter and Spacing on Implosion Resistance of Ultra-High Performance Concrete. *Eng. Mech.* **2023**, *40*, 98–107.
- Lu, H.; Yue, S.; Sun, S.; Song, C.; Xiong, Z. Model test study on damage depth of concrete target under penetration and explosion. *Explos. Shock Waves* **2021**, *41*, 073301–1.
- Westine, P.S.; SOUTHWEST RESEARCH INST SAN ANTONIO TX. *Bomb Crater Damage to Runways*; Air Force Weapons Laboratory: Dayton, OH, USA, 1973; p. 0091.
- Wang, Q.; Gu, W.; Xia, W. An experimental study on damage effect caused by an explosion in multilayer medium. *Chin. J. Eng. Blasting* **2003**, *2*, 7.
- Wei, W.L.; Chen, Y.Q.; Wang, Z.Q.; Li, S.T.; Chen, L.M.; Huang, C.L. Comparative study on damage effects of penetration and explosion modes on airport runway. *Constr. Build. Mater.* **2024**, *411*, 134169. [[CrossRef](#)]
- Forrestal, M.J.; Altman, B.S.; Cargile, J.D.; Hanchak, S.J. An empirical equation for penetration depth of ogive-nose projectiles into concrete targets. *Int. J. Impact Eng.* **1994**, *15*, 395–405. [[CrossRef](#)]
- Shu, Y.; Wang, G.; Lu, W.; Chen, M.; Lv, L.; Chen, Y. Damage characteristics and failure modes of concrete gravity dams subjected to penetration and explosion. *Eng. Fail. Anal.* **2022**, *134*, 106030. [[CrossRef](#)]
- Han, J.; Kim, S.; Hwang, I. Numerical Assessment and Repair Method of Runway Pavement Damage Due to CBU Penetration and Blast Loading. *Appl. Sci.* **2022**, *12*, 2888. [[CrossRef](#)]
- Osborne, D.T.; Pantoya, M.L. Effect of Al particle size on the thermal degradation of Al/Teflon mixtures. *Combust. Sci. Technol.* **2007**, *179*, 1467–1480. [[CrossRef](#)]
- Saikov, I.; Seropyan, S.; Malakhov, A.; Saikova, G.; Denisov, I.; Petrov, E. Energetic Materials Based on W/PTFE/Al: Thermal and Shock-Wave Initiation of Exothermic Reactions. *Metals* **2021**, *11*, 1355. [[CrossRef](#)]
- Casem, D.T.; Casem, D.T. *Mechanical Response of an Al-PTFE Composite to Uniaxial Compression over a Range of Strain Rates and Temperatures*; Army Research Laboratory: Adelphi, MD, USA, 2008.
- Speerschneider, C.J.; Li, C.H. A correlation of mechanical properties and microstructure of polytetrafluoroethylene at various temperatures. *J. Appl. Phys.* **1963**, *34*, 3004–3007. [[CrossRef](#)]
- Ames, R. Vented chamber calorimetry for impact-initiated energetic materials. In *Proceedings of the 43rd AIAA Aerospace Sciences Meeting and Exhibit, Reno, Nevada, 10–13 January 2005*; p. 279.
- Rosencrantz, S.D. *Characterization and Modeling Methodology of Polytetrafluoroethylene Based Reactive Materials for the Development of Parametric Models*. Ph.D. Thesis, Wright State University, Dayton, OH, USA, 2007.

21. Daniels, A.; Baker, E.; Ng, K. A unitary demolition warhead. In Proceedings of the Mines, Demolition and Non-Lethal Weapons Conference, New Orleans, LA, USA, 11 September 2003.
22. Daniels, A.S.; Baker, E.L.; DeFisher, S.E.; Ng, K.W.; Pham, J. Bam bam: Large scale unitary demolition warheads. In Proceedings of the 23rd International Symposium on Ballistics, Tarragona, Spain, 16–20 April 2007; pp. 16–20.
23. Xiao, J.; Zhang, X.; Wang, Y.; Xu, F.; Wang, H. Demolition mechanism and behavior of shaped charge with reactive liner. *Propellants Explos. Pyrotech.* **2016**, *41*, 612–617. [[CrossRef](#)]
24. Xiao, J.; Zhang, X.; Guo, Z.; Wang, H. Enhanced Damage Effects of Multi-Layered Concrete Target Produced by Reactive Materials Liner. *Propellants Explos. Pyrotech.* **2018**, *43*, 955–961. [[CrossRef](#)]
25. ZHANG, X.P.; XIAO, J.G.; YU, Q.B.; ZHENG, Y.F.; WANG, H.F. Demolition effect of reactive material liner shaped charge against concrete target. *Trans. Beijing Inst. Technol.* **2016**, *36*, 1211–1215.
26. Zheng, Y.F.; Su, C.H.; Guo, H.G.; Yu, Q.B.; Wang, H.F. Chain damage effects of multi-spaced plates by reactive jet impact. *Def. Technol.* **2021**, *17*, 393–404. [[CrossRef](#)]
27. Chenghai, S.U.; Zongyu, L.L.; Yuanfeng, Z.H.E.N.G.; Zhijian, Z.H.E.N.G.; Huanguo, G.U.O. Penetration-deflagration Experiment and Coupling Mechanism of Reactive Liner Shaped Charge. *Acta Armamentarii* **2023**, *44*, 334.
28. Baum, F.A.; Orlenko, L.P.; Stanyukovich, K.P.; Chelyshev, V.P.; Shekhter, B.I. *Physics of an Explosion*; Department of the Army, Corps of Engineers: Washington, DC, USA, 1963.
29. Tu, Z.; Lu, Y. Modifications of RHT material model for improved numerical simulation of dynamic response of concrete. *Int. J. Impact Eng.* **2010**, *37*, 1072–1082. [[CrossRef](#)]
30. Leppänen, J. Concrete subjected to projectile and fragment impacts: Modelling of crack softening and strain rate dependency in tension. *Int. J. Impact Eng.* **2006**, *32*, 1828–1841. [[CrossRef](#)]
31. Malvar, L.J.; Crawford, J.E.; Wesevich, J.W.; Simons, D. A plasticity concrete material model for DYNA3D. *Int. J. Impact Eng.* **1997**, *19*, 847–873. [[CrossRef](#)]
32. Malvar, L.J.; Crawford, J.E.; Morrill, K.B. K&C concrete material model release III-automated generation of material model input. In *Karagozian and Case Structural Engineers*; Technical Report TR-99-24.3; Glendale, CA, USA, 18 August 2000.
33. Hu, R.; Jiang, C.; Lu, G.; Wang, Z.; Mao, L. Damage Effects and Engineering Computational Model of Internal Explosion of Airfield Runway. *Acta Armamentarii* **2023**, *44*, 929.
34. Raftenberg, M.N.; Mock Jr, W.; Kirby, G.C. Modeling the impact deformation of rods of a pressed PTFE/Al composite mixture. *Int. J. Impact Eng.* **2008**, *35*, 1735–1744. [[CrossRef](#)]
35. Ren, S.; Zhang, Q.; Wu, Q.; Long, R.; Gong, L.; Lu, Y. A reactive material double-bumper shield for centimeter sized projectile. *Int. J. Impact Eng.* **2021**, *158*, 104028. [[CrossRef](#)]
36. Xiao, Q.Q.; Huang, Z.X.; Jia, X.; Zu, X.D.; Zhu, Q.F. Shaped charge penetrator into soil–concrete double-layered target. *Int. J. Impact Eng.* **2017**, *109*, 302–310. [[CrossRef](#)]
37. Xiao, J.G. *Research on Damage Effects of Multi-Layered Concrete Targets Impacted by Explosively Formed Penetrator*; Beijing Institute of Technology: Beijing, China, 2016.

**Disclaimer/Publisher’s Note:** The statements, opinions and data contained in all publications are solely those of the individual author(s) and contributor(s) and not of MDPI and/or the editor(s). MDPI and/or the editor(s) disclaim responsibility for any injury to people or property resulting from any ideas, methods, instructions or products referred to in the content.